

Optimisation of PET Image Reconstruction: Use of Neural Networks for Scatter Estimation

Adil Bardane^{1*}, El Mahjoub Chakir¹, El mehdi Al Ibrahmi¹, Hassane El Bekkouri¹

¹Department of Physics Laboratory of Materials Physics and Subatomic, Faculty of Sciences, Ibn Tofail University, Street, Kenitra, Morocco.

*Corresponding author(s). E-mail(s): adil.bardane@uit.ac.ma; Contributing authors: mahchakir@yahoo.fr; alibrahmi.elmehdi@uit.ac.ma; hassane.elbekkouri@uit.ac.ma;

Abstract

This study aims to exploit neural networks to develop innovative methods for estimating diffusion, improving the accuracy/computation time ratio in the PET (Positron Emission Tomography) image reconstruction process. The methodology is based on Monte-Carlo simulations, which have been used to generate a large set of realistic PET data, essential for training neural networks. Detailed modelling of tomographs and analytical phantoms with a variety of characteristics was used to create a substantial learning base. The results show a significant improvement in the accuracy of reconstructions while significantly reducing computing time, demonstrating the potential of neural network-based approaches for optimising reconstruction processes in medical imaging.

Keywords: Monte Carlo simulation; GATE;PET-scan; Machine Learning;U-Net;ReLU;OSEM;

1 Introduction

PET is an imaging technique used to observe and quantify biological processes by estimating the distribution of molecules labelled with radioactive elements, known as radiotracers [1–3]. This modality, based on the principle of scintigraphy, is said to be functional because it allows us to observe metabolism, as opposed to so-called anatomical imaging, which allows us to observe the structures of different tissues[4].

As anatomical and functional information are complementary, PET is often combined with other anatomical imaging modalities to take advantage of enriched information when reconstructing the data acquired, or even when interpreting the final images. These are known as hybrid or bimodal systems, such as PET/CT or PET/MRI[5–10].

The use of the detection time of annihilation photons in PET, known as the Time of Flight (TOF), makes it possible to delimit the origin of the radiotracer more precisely [11]. This delineation offers a multitude of advantages, including noise reduction, artefact attenuation and acceleration of iterative methods [12]. In addition, a TDV resolution, also known as temporal resolution, better than 30 picoseconds (ps), which we will call ultra-precise TDV for short, would allow, for clinical-size cameras, direct image formation with a spatial resolution equivalent to that obtained by iterative reconstruction methods [13–15]. Currently, the best TDV resolution available in a clinical PET camera is close to 200 ps, which corresponds to a spatial accuracy of 30 mm [16]. In 2020, a temporal resolution of 58 ps was achieved with PET detectors using an optimised test bench. Various avenues have been considered for achieving ultra-precise CT [17, 18]. A challenge has even been formally established around this objective. Despite this, there is no consensus in the scientific community on the relevance and feasibility of achieving such a high-resolution TDV since some of the avenues considered would affect other camera performance parameters, e.g. detector sensitivity [19, 20]. However, many factors can, in varying proportions, disturb the signal and affect the image qualitatively and quantitatively. These factors may be linked to the physical interactions of the particles involved, the intrinsic limitations of the imaging system, or extrinsic disturbances such as the patient's cardiac or respiratory movements. Among these factors, scattering and attenuation phenomena, linked to the Compton interactions of photons as they propagate through tissues, can lead to significant contrast losses in regions of heterogeneous density and activity [21].

This can lead to biases in quantification, and may even create artefacts in the final image that could affect its interpretation. What's more, with three-dimensional (3- D) PET systems, which are increasingly being used to replace two-dimensional (2-D) systems, the impact of the scattering phenomenon is all the greater, with scattered coincidences accounting for up to 50% of the total coincidences detected [22]. It is therefore crucial to correct this by taking it into account in the image reconstruction process [23]. Attenuation correction in routine clinical practice is commonly carried out based on anatomical information acquired by hybrid PET-CT systems. The increasing use of PET-Magnetic Resonance Imaging (MRI) systems, due to their diagnostic interest, has necessitated the development of attenuation correction methods based on MRI images [8]. However, attenuation correction using structural acquisitions coupled with PET acquisition is not optimal. Anatomical images can suffer from registration errors on the

PET image, and artefacts can propagate to the final image during the reconstruction process. The most promising approach for single-modality PET and PET-MRI systems today seems to be to correct attenuation by using only the emission data [24]. Recent work on this subject shows encouraging results but needs to be further validated.

Deep learning is an AI approach based on the use of neural networks. The concept of artificial neural networks was born in the late 1940s, based on an analogy with the

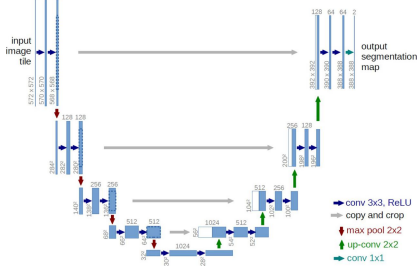


Fig. 1: U-Net architecture for medical image segmentation [27]

biological neural networks of the brain, with the idea of equalling or even surpassing human performance [25]. However, the initial algorithms were too simplistic, and the lack of data and IT resources meant that the hoped-for objectives could not initially be achieved[26]. Over the past 10 years, the exploitation of massive data ("big data"), and technical advances offering increased computing possibilities (GPUs, computing grids or "clusters"), have led to a sharp upsurge in the use of this type of method and the development of the underlying algorithms. These methods offer new solutions for solving complex problems. As a result, deep learning is gradually finding applications in a wide range of fields: automotive, industry, health, robotics, economics, agriculture, etc. At the heart of deep learning techniques, neural networks particularly CNNs are being adapted to image interpretation. AI has thus largely found its place in the field of medical imaging, and neural networks are used in many PET imaging applications[28]. This paper presents the Monte Carlo simulation methodology used to generate a large set of realistic PET data, necessary for the use of neural networks. The modelling of two tomographs and anthropomorphic phantoms with a variety of characteristics gives us a substantial learning base for the methods we have developed. Finally, we propose respective methods for estimating diffusion and attenuation, based on deep learning techniques.

2 Materials and Methods

2.1 Monte carlo simulation

Geant4 Application for Tomography Emission (GATE) is a software package dedicated to digital simulations in medical imaging. Initiated in 2002 by the OpenGATE collaboration (25 institutions are involved in its development (laboratories, companies, medical centres)), and published in 2004 [29], it is written in C++, open source, and still actively maintained. GATE encapsulates the GEANT4 libraries to provide a modular and flexible medical imaging simulation tool. Its user interface is simplified, based on command calls, used interactively or via macro

files containing a list of commands. It can be used to simulate PET, SPECT and CT systems, and to carry out radiotherapy 10 experiments. It is an essential tool for developing new imaging

systems, experimenting with new protocols, and developing new reconstruction and correction methods [30].

2.1.1 Geometric

model Phantom

We simulated a dataset using cylindrical phantoms. Homogeneous spheres of 2 different sizes and materials were generated with a random voxel from an image of 256² positioned at the centre of the cylinder (Fig2).

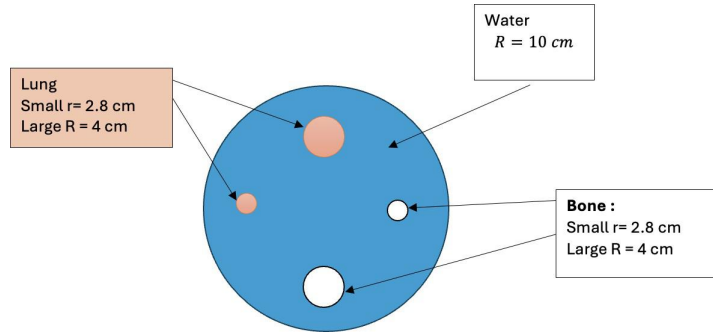


Fig. 2: simulated cylinder (20 cm radius and 20 cm height) contains 2 spheres of bone and 2 of Lung ($R = 4$ cm and $r = 2.8$ cm)

PET Scan

In this work, we based ourselves on the ECAT EXACT HR^+ from Simens. These geometric characteristics are listed in Tabl1.

Parameters for considered PET scanners	ECAT EXACT HR^+
Detector ring diameter	82.4 mm
Axial field of view	155 mm
Detector material	Bismuth germinate
(BGO) Crystal dimensions mm	$4.05 \times 4.39 \times 30$
Total number of crystals	
18432 Number of crystals per detector block	256
Number of detector rings	72
Energy window keV	300-650
Coincidence window	12 ns

Table 1: Features of the ECAT EXACT HR^+ PET scanners

To overcome the slowness of Monte Carlo simulations, we are exploiting the parallel computing capabilities of the HPC-MARWAN grid at our

disposal. The grid can be

used to manage the allocation of resources according to the needs of the tasks to be executed (number of CPUs required, need for one or more GPUs), and to manage the executions in progress.

The simulation of an acquisition lasting T is thus broken down into multiple acquisitions from time t to $t+x$, with $t \in [0, x, 2x, \dots, T-x]$. The simulation time is therefore proportional to the duration x of each acquisition if the necessary resources are available, the aim being to minimise x and to divide the simulations into as many subsets as possible.

In one of his publications [31], C. Schmidlein describes a method for determining the sinogram index corresponding to each LOR, from the indexes of the pairs of crystals involved. The azimuthal bin i of the Φ axis of the sinogram is determined by :

$$i = Crystal_1 + Crystal_2 + c \quad (1)$$

where $Crystal_1$ and $Crystal_2$ are the identifiers of the 2 crystals involved in the LOR under consideration and indexed as described by C. Schmidlein, and c is the arbitrary offset that satisfies the condition $\Phi = 0$, with :

$$\frac{\Phi}{2\pi_i} = i/N \quad (2)$$

N being the number of crystals per ring, and $i \in [0, N/2]$. The index j of the radial axis r of the sinogram is determined according to the radial distance of the LOR under consideration from the centre of the tomograph. It is calculated by :

$$|j| = \frac{N}{2} - |Crystal_1 - Crystal_2| \quad (3)$$

$$j = \begin{cases} +|j| & \text{if } Crystal_{1,2} \in [i, i + \frac{N}{2}] \\ -|j| & \text{otherwise} \end{cases} \quad (4)$$

The sign of j is determined by the position of the LOR relative to Φ :

Finally, the index of the LORs along the last axis θ of the sinogram is simply classified from the axial position of the rings $A1$ and $A2$ to which the crystals $Crystal_1$ and $Crystal_2$ belong and the LOR under consideration, and their index difference:

$$\text{Ring Difference} = |A1 - A2|$$

2.2 Network Framework

2.2.1 Neural network architecture

The method developed proposes to use neural networks to estimate diffusion from sinogram space, before the actual reconstruction stage. It is based on a U-Net architecture which takes as input the slices of the 3-D emission and attenuation sinograms, to predict as output the

corresponding slice of the scattering sinogram. The architecture of the network is illustrated in Fig.3.

The input emission and attenuation sinograms are first concatenated before being injected into the convolutional part of the U-Net network, consisting of 5 successive

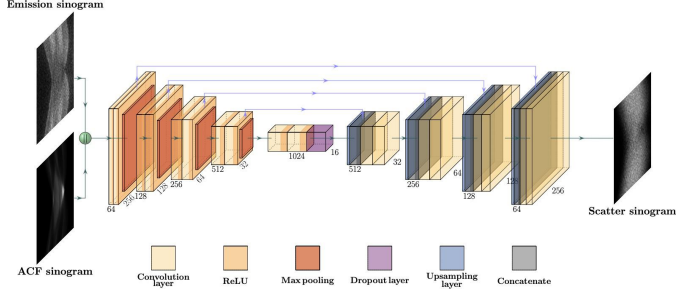


Fig. 3: Architecture of the DLSE network, taking emission and attenuation sinograms as input. The data undergoes a series of convolutions to extract its characteristics, and then a series of deconvolutions to recover the original spatial information and dimensions. The predicted output is the scattering sinogram.

convolution layers. Each of these 5 convolution layers consists of two convolution operations followed by a ReLU activation function and a max-aggregation operation with a kernel of size 2 × 2. A dropout layer is added at the end of the convolutional part, to reduce the risk of overlearning [3]. The second part of the network performs deconvolution operations to recover the spatial resolution of the input data. This so-called expansive part is similar to the contracting part, except that the max-aggregation operations are replaced by oversampling operations using the nearest neighbours method, with a kernel of size 2 × 2. The output scattering sinogram has the same dimensions as the input sinograms. Connections between convolution layers and deconvolution layers of the same level are used to recover spatial information that may be lost during convolution operations.

The loss function used is the mean square error (MSE), defined as follows:

$$MSE = \frac{1}{n} \sum_{i=1}^n (x_i - y_i)^2 \quad (5)$$

$x = [x_1, \dots, x_n] \in \mathbb{R}^n$ being the scattering sinogram derived from the ground truth, $y = [y_1, \dots, y_n] \in \mathbb{R}^n$ the predicted diffusion sinogram, with n the number of pixels of the sinograms, with x_i and y_i being the ground truth data and the predicted data respectively.

The Adam optimizer is used to minimize the loss function. Its learning rate has been set at 10^{-5} , and the batch size at 8. To avoid overlearning, a premature stop criterion terminates learning if the loss function does not decrease over 10 consecutive epochs. The input and output sinograms (for the training phase) are normalised [7], and resized so that their dimensions are a multiple of 2^5 , 5 being the number of convolution layers making up the contracting part of the network. This CNN was implemented using the Keras framework [5] as an overlay for the

Tensorflow platform [9].

2.3 Data Generation and Training

Each 3-D sinogram triplet (emission, attenuation and scattering) obtained from the MC simulations consists of 837 slices, representing a total dataset of around 20,000 slices respectively. This data was distributed as follows: 2/3 of each dataset was allocated to the network training stage, 1/6 to the validation stage, and the remaining 1/6 to the test stage.

To evaluate the results objectively, we used 2 metrics, namely the NRMSE and the scatter ratio accuracy (SRA), defined as :

$$NRMSE = \frac{\sqrt{MSE}}{y_{max} - y_{min}} \quad (6)$$

MSE defined in equation 5 and :

$$SRA = 100 - Relative - Error_{x,y} \quad (7)$$

with :

$$Relative - Error_{x,y} = \frac{|Scatter - Ratio_x - Scatter - Ratio_y|}{Scatter - Ratio_y} \times 100 \quad (8)$$

And,

$$Scatter - Ratio_x = \frac{NumberOfScatteredEvents_x}{TotalNumberOfEvents} \quad (9)$$

With $x = [x_1, \dots, x_m] \in \mathbb{R}^n$ and $y = [y_1, \dots, y_n] \in \mathbb{R}^n$ being respectively the ground truth and the predicted data, ScatterRatio the percentage of scattered events relative to the total number of events, y_{max} and y_{min} corresponding respectively to the maximum and minimum intensity values of y , and m the number of pixels. The combination of these two metrics enables us to carry out an objective evaluation, taking into account both the intensity and the location of the scattered coincidences in sinogram space.

To evaluate the performance of the deep learning-based scatter estimation (DLSE) method from a quantitative point of view, we propose to compare its performance against the SSS scatter estimation method and the ground truth from the mMR simulations. To do this, we reconstructed simulated mMR data by injecting the various scattering sinograms estimated by our method, as well as the two comparison methods, during the reconstruction.

The NRMSE and structural similarity index measure (SSIM)[3] values of the reconstructed images are then calculated, along with the contrast C of each lesion relative to the surrounding tissue, defined as :

$$C = \frac{\frac{1}{\#L} \sum_{j \in L} x_j}{\frac{1}{\#B} \sum_{j \in B} x_j} \quad (10)$$

with $x = [x_1, \dots, x_n] \in \mathbb{R}^n$ the reconstructed image, j the voxels in the image, L and B the subsets of voxels corresponding to the lesions and surrounding tissue respectively, and $\#L$ and $\#B$ the number of voxels in each subset.

3 Results

Fig.4 shows the evolution of the loss functions for the training and validation data and allows us to observe their convergence. In this case, the early stopping criterion stopped the training phase after 72 epochs. The prediction of a single slice of the ECAT scattering sinogram takes 30 ms, which represents 16 seconds to predict a complete scattering sinogram of 553 slices.

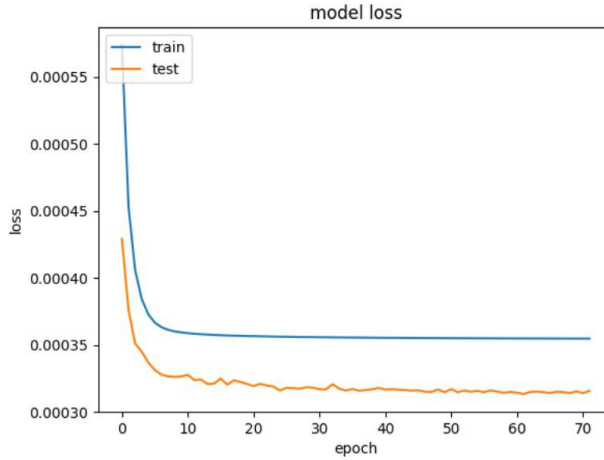
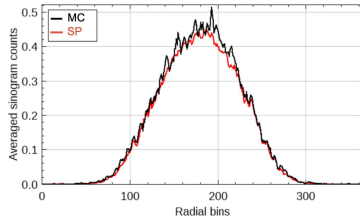
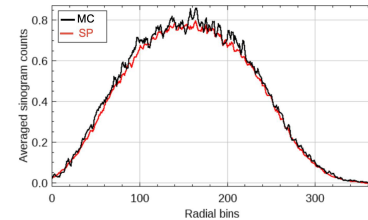


Fig. 4: Convergence of the model's MSE loss function during the training and validation stages applied to the full dataset.

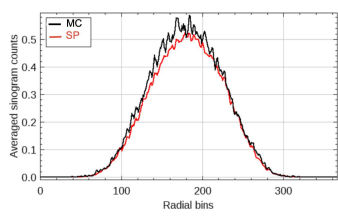


(a) Small sphere

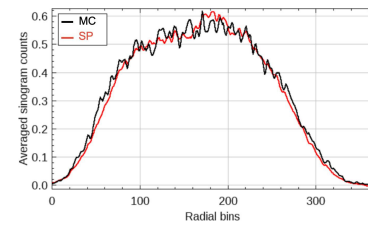


(b) Large sphere

Fig. 5: The corresponding line profile scattering predicted (SP) by the DLSE method is then compared with the ground truth (MC) of the Monte Carlo simulation for Bone materials of small and large sizes.



(a) Small sphere



(b) Large sphere

Fig. 6: The corresponding line profile scattering predicted (SP) by the DLSE method is then compared with the ground truth (MC) of the Monte Carlo simulation for lung materials of small and large sizes.

Fig. 7 shows the NRMSE values for datasets of different acquisition times, being trained and tested independently. As expected, the DLSE method performs better as the statistical quality of the data increases. The values decrease linearly as the acquisition time increases.

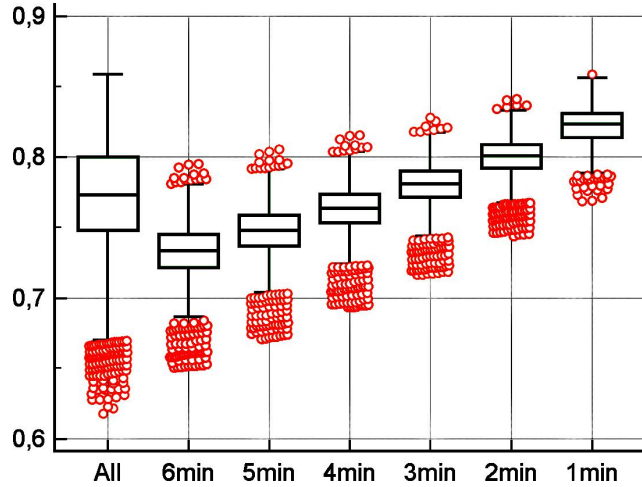
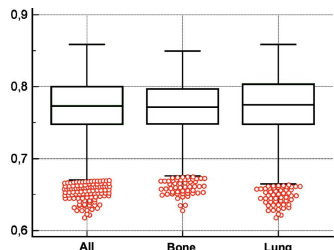
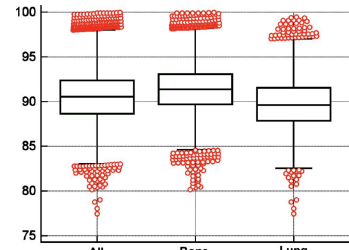


Fig. 7: NRMSE values in the face of variations in the statistical level of the data due to simulation times. Comparison of the DLSE method with the MC ground truth.

The graph in Fig.8 shows the quantitative results obtained for the 2 anatomical regions studied. The mean NRMSE values for the lung and bone regions are 0.7750 and 0.7721 respectively, while the SRA values are 89.37 ± 2.68 and 91.41 ± 2.72 respectively.



(a) NRMSE



(b) SRA

Fig. 8: Results on the 2 different anatomical volumes (lung and bone), and comparison of the DLSE method with the MC ground truth. The network was trained on the entire training set, including all phantom materials.

The results concerning the influence of size on these 2 regions independently show a stable NRMSE for the 2 different sizes considered. For the Bone region, the maximum variations in the mean NRMSE

compared with the results from the complete Bone dataset do not exceed 1.5% for the 2 sizes and are less than 0.6% for the Lung region.

For these 2 regions, the SRA increases with the size of the phantom. For the Bone, the mean SRA is 89.51% and 93.51% respectively for fine and large spheres (see table 2).

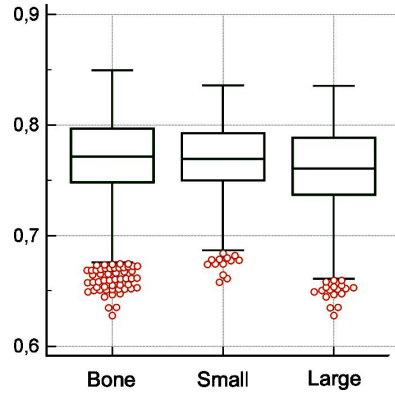
Metric		Bone	Small sphere	Large sphere
Scatter ratio accuracy	Mean	91.41	89.51	91.20
	STD	2.72	2.31	2.27
NRMSE	Mean	0.7721	0.7104	0.7838
	STD dev	0.0332	0.028	0.0337

Table 2: Results of the DLSE method on Bone data, according to the sphere's size, compared with the MC ground truth. The network is trained on the full training dataset.

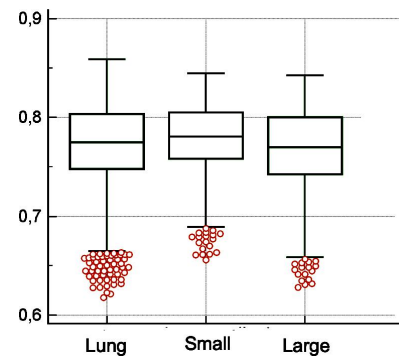
This corresponds to variations of -2.08% and +2.30% compared with the mean SAR values for the full Bone dataset. For the lung region, these variations are -2.12% and +2.59% respectively for small and wide sizes (calculated from the data in Table 3).

Metric		Lung	Small sphere	Large sphere
Scatter ratio accuracy	Mean	89.71	87.81	92.03
	STD	2.68	2.17	2.00
NRMSE	Mean	0.7750	0.7811	0.7732
	STD	0.0367	0.0304	0.0410

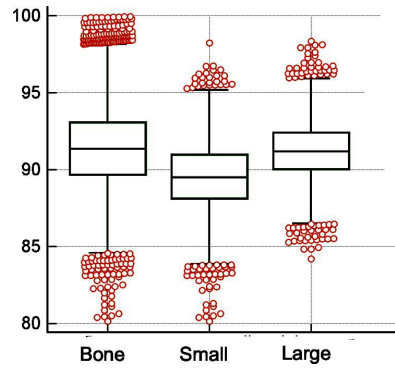
Table 3: Results of the DLSE method on lung data, according to the sphere's size, compared with the MC ground truth. The network is trained on the full training dataset.



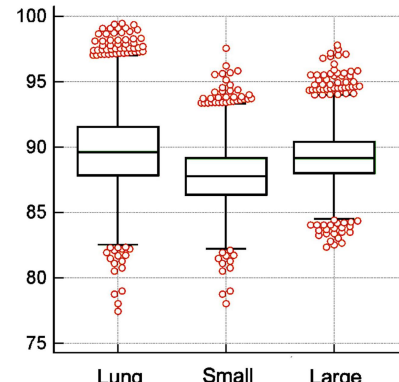
(a) NRMSE-Bone



(b) NRMSE-Lung



(c) SRA-Bone



(d) SRA-Lung

Fig. 9: Results for variations in phantom size of spheres, and comparison of the production method (DLSE) with the MC ground truth. The network was trained on the entire training set, including all spheres.

4 Conclusion

This study developed neural network-based methods to enhance the estimation of scatter and attenuation in PET image reconstructions, using Monte Carlo simulations to generate a large dataset of PET sinograms for model training. The neural networks demonstrated improved accuracy in predicting these effects, resulting in higher quality reconstructed images with reduced noise and artifacts, crucial for accurate disease diagnosis and monitoring.

A significant benefit of this approach is the reduction in computation time, making it practical for clinical use by enabling the processing of large data volumes in real-time. This capability is particularly valuable for monitoring treatments and assessing therapeutic responses.

The study also highlights the utility of Monte Carlo simulations in generating diverse data for training machine learning models in medical imaging, which enhances the models' robustness and generalizability.

Overall, this research marks a notable advancement in using neural networks for PET imaging, offering promising implications for other imaging modalities and clinical applications.

References

- [1] Gawne, P.J., Man, F., Blower, P.J., Rosales, R.: Direct cell radiolabeling for in vivo cell tracking with pet and spect imaging. *Chemical reviews* **122**(11), 10266– 10318 (2022)
- [2] Slart, R.H., Williams, M.C., Juarez-Orozco, L.E., Rischpler, C., Dweck, M.R., Glaudemans, A.W., Gimelli, A., Georgoulias, P., Gheysens, O., Gaemperli, O., et al.: Position paper of the eacvi and eanm on artificial intelligence applications in multimodality cardiovascular imaging using spect/ct, pet/ct, and cardiac ct. *European journal of nuclear medicine and molecular imaging* **48**, 1399–1413 (2021)
- [3] Crisan, G., Moldovean-Cioroianu, N.S., Timaru, D.-G., Andries, , G., Căinap, C., Chis, , V.: Radiopharmaceuticals for pet and spect imaging: a literature review over the last decade. *International journal of molecular sciences* **23**(9), 5023 (2022)
- [4] Hussain, S., Mubeen, I., Ullah, N., Shah, S.S.U.D., Khan, B.A., Zahoor, M., Ullah, R., Khan, F.A., Sultan, M.A.: Modern diagnostic imaging technique applications and risk factors in the medical field: a review. *BioMed research international* **2022**(1), 5164970 (2022)
- [5] Al-Sharify, Z.T., Al-Sharify, T.A., Al-Sharify, N.T., et al.: A critical review on medical imaging techniques (ct and pet scans) in the medical field. In: IOP Conference Series: Materials Science and Engineering, vol. 870, p. 012043 (2020). IOP Publishing
- [6] Overcast, W.B., Davis, K.M., Ho, C.Y., Hutchins, G.D., Green, M.A., Graner, B.D., Veronesi, M.C.: Advanced imaging techniques for neuro-oncologic tumor diagnosis, with an emphasis on pet-mri imaging of malignant brain tumors. *Current Oncology Reports* **23**, 1–15 (2021)
- [7] Verweij, N.J., Yaqub, M., Bruijnen, S.T., Pieplenbosch, S., Ter Wee, M.M., Jansen, G., Chen, Q., Low, P.S., Windhorst, A.D., Lammertsma, A.A., et al.: First in man study of [18f] fluoro-peg-

folate pet: a novel macrophage imaging

- technique to visualize rheumatoid arthritis. *Scientific reports* **10**(1), 1047 (2020)
- [8] Oostveen, W.M., Lange, E.C.: Imaging techniques in alzheimer's disease: a review of applications in early diagnosis and longitudinal monitoring. *International journal of molecular sciences* **22**(4), 2110 (2021)
- [9] Castellano, A., Bailo, M., Cicone, F., Carideo, L., Quartuccio, N., Mortini, P., Falini, A., Cascini, G.L., Minniti, G.: Advanced imaging techniques for radiotherapy planning of gliomas. *Cancers* **13**(5), 1063 (2021)
- [10] Tanaka, T., Yang, M., Froemming, A.T., Bryce, A.H., Inai, R., Kanazawa, S., Kawashima, A.: Current imaging techniques for and imaging spectrum of prostate cancer recurrence and metastasis: a pictorial review. *Radiographics* **40**(3), 709– 726 (2020)
- [11] Sarrut, D., Etxebeste, A., Muñoz, E., Krah, N., Létang, J.M.: Artificial intelligence for monte carlo simulation in medical physics. *Frontiers in Physics* **9**, 738112 (2021)
- [12] Trigila, C., Srikanth, A., Roncali, E.: A generative adversarial network to speed up optical monte carlo simulations. *Machine Learning: Science and Technology* **4**(2), 025005 (2023)
- [13] Schäfer, V.S., Jin, L., Schmidt, W.A.: Imaging for diagnosis, monitoring, and outcome prediction of large vessel vasculitides. *Current rheumatology reports* **22**, 1–14 (2020)
- [14] Gomes, A., Geel, P.P., Santing, M., Prakken, N.H., Ruis, M.L., Assen, S., Slart, R.H., Sinha, B., Glaudemans, A.W.: Imaging infective endocarditis: Adherence to a diagnostic flowchart and direct comparison of imaging techniques. *Journal of Nuclear Cardiology* **27**(2), 592–608 (2020)
- [15] Mathew, R.C., Bourque, J.M., Salerno, M., Kramer, C.M.: Cardiovascular imaging techniques to assess microvascular dysfunction. *Cardiovascular Imaging* **13**(7), 1577–1590 (2020)
- [16] Liu, J., Sun, X., Li, R., Peng, Y.: Recognition of cervical precancerous lesions based on probability distribution feature guidance. *Current Medical Imaging* **18**(11), 1204–1213 (2022)
- [17] Lai, L.-Y., Jiang, Y., Shu, J.: The application of dual-layer spectral detector ct in abdominal vascular imaging. *Current Medical Imaging* **19**(14), 1609–1615 (2023)
- [18] Sarrut, D., Etxebeste, A., Muñoz, E., Krah, N., Létang, J.M.:

Artificial intelligence for monte carlo simulation in medical physics.
Frontiers in Physics 9, 738112 (2021)

- [19] Houssein, E.H., Abohashima, Z., Elhoseny, M., Mohamed, W.M.: Machine learning in the quantum realm: The state-of-the-art, challenges, and future vision. *Expert Systems with Applications* **194**, 116512 (2022)
- [20] Bardane, A., Tajmouati, J., Maghnouj, A., Dadouch, A.: Monte carlo simulation method highlighting on the electron beam irradiation on the structure of sars- cov-2. *Moscow University Physics Bulletin* **75**(6), 638–644 (2020)
- [21] Mukku, L., Thomas, J.: Advanced cervical lesion detection using deep learning techniques. In: 2024 1st International Conference on Communications and Computer Science (InCCCS), pp. 1–6 (2024). IEEE
- [22] Trigila, C., Srikanth, A., Roncalli, E.: A generative adversarial network to speed up optical monte carlo simulations. *Machine Learning: Science and Technology* **4**(2), 025005 (2023)
- [23] Gianani, I., Mastroserio, I., Buffoni, L., Bruno, N., Donati, L., Cimini, V., Bar- bieri, M., Cataliotti, F.S., Caruso, F.: Experimental quantum embedding for machine learning. *Advanced Quantum Technologies* **5**(8), 2100140 (2022)
- [24] Markfort, A., Baranov, A., Conneely, T., Duran, A., Lapington, J., Milnes, J., Mudrov, A., Tyukin, I.: Investigating machine learning solutions for high-speed data analysis and imaging of a single photon counting detector with picosecond timing resolution. In: 2021 IEEE Nuclear Science Symposium and Medical Imaging Conference (NSS/MIC), pp. 1–4 (2021). IEEE
- [25] Bellens, S., Guerrero, P., Vandewalle, P., Dewulf, W.: Machine learning in industrial x-ray computed tomography—a review. *CIRP Journal of Manufacturing Science and Technology* **51**, 324–341 (2024)
- [26] Shukrun, R., Shwartz, S., et al.: Monte carlo simulations for ghost imaging based on scattered photons. *arXiv preprint arXiv:2306.16702* (2023)
- [27] Kiruba, B., Raja, M.M., Jeya, I.J.S., Angel, C.: A perspective study on quantum machine learning models for the areas of medicine, materials, sensing, and communication. *Quantum Computing and Artificial Intelligence: Training Machine and Deep Learning Algorithms on Quantum Computers*, 205 (2023)
- [28] Bellens, S., Guerrero, P., Vandewalle, P., Dewulf, W.: Machine learning in industrial x-ray computed tomography—a review. *CIRP Journal of Manufacturing Science and Technology* **51**, 324–341

(2024)

- [29] Grevillot, L., Boersma, D., Fuchs, H., Aitkenhead, A., Elia, A., Bolsa, M., Win- terhalter, C., Vidal, M., Jan, S., Pietrzyk, U., *et al.*: Gaterion: a gate/geant4 release for clinical applications in scanned ion beam therapy. *Medical Physics* **47**(8), 3675–3681 (2020)

- [30] Overcast, W.B., Davis, K.M., Ho, C.Y., Hutchins, G.D., Green, M.A., Graner, B.D., Veronesi, M.C.: Advanced imaging techniques for neuro-oncologic tumor diagnosis, with an emphasis on pet-mri imaging of malignant brain tumors. *Current Oncology Reports* **23**, 1–15 (2021)
- [31] Schmidlein, C.R., Kirov, A.S., Nehmeh, S.A., Erdi, Y.E., Humm, J.L., Amols, H.I., Bidaut, L.M., Ganin, A., Stearns, C.W., McDaniel, D.L., et al.: Validation of gate monte carlo simulations of the ge advance/discovery ls pet scanners. *Medical physics* **33**(1), 198–208 (2006)